ACS Photonics

Article

pubs.acs.org/journal/apchd5

# Engineering Near-Field SEIRA Enhancements in Plasmonic Resonators

Jungseok Chae,[†,‡] Basudev Lahiri,[†,‡] and Andrea Centrone*[,†]

[†]Center for Nanoscale Science and Technology, National Institute of Standards and Technology 100 Bureau Drive, Gaithersburg, Maryland 20899, United States

[‡]Maryland Nanocenter, University of Maryland, College Park, Maryland 20742, United States

Supporting Information

**ABSTRACT:** Engineering of the optical resonances in plasmonic resonator arrays is achieved by virtue of the intrinsic properties of the constituent structures such as composition, size, and shape and by controlling the inter-resonator interactions by virtue of the array's geometrical arrangement. The nanoscale confinement of the plasmonic field enhances light−matter interactions, enabling, for instance, the surface-enhanced infrared absorption (SEIRA) effect. However, the subwavelength confinement also poses an experimental challenge for discriminating the response stemming from the individual resonators and from the collective response in densely packed arrays. In this work, the photothermal induced resonance technique is leveraged to obtain nanoscale images and spectra of near-field SEIRA hot spots observed in isolated plasmonic resonators of different shapes and in selected resonators within closely packed plasmonic arrays, informing on whether the interactions with neighboring resonators are beneficial or otherwise. Results are correlated with far-field spectra and theoretical calculations.

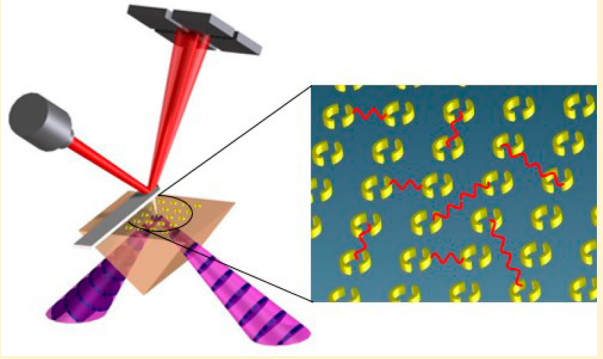

**KEYWORDS:** *plasmonic materials, split ring resonators, SEIRA, PTIR*

Metamaterials are artificially engineered materials that derive their properties from a combination of composition and structure, rather than from composition alone.[1−6] Metamaterials attract great interest because they exhibit electromagnetic properties that differ from those of naturally occurring materials. For example, the interplay between composition and structure allows bending electromagnetic waves at arbitrary angles and engineering the permittivity ($\varepsilon$) and the permeability ($\mu$) of those constructs.[1−5] Such unique properties enable a plethora of applications hitherto unavailable such as perfect lenses,[3] electromagnetic cloaks,[4] and miniaturized antennas.[6] Among metamaterials, split ring resonators (SRRs) consist of a metallic loop with one or more gaps (see Figure 1a) and are among the most studied nanostructures. It is well known that SRRs and other plasmonic materials display wavelength-tunable resonances as a function of size and shape.[5−9] Plasmonic resonances have the merit of confining light to nanoscale volumes of matter (hot spots), resulting in locally enhanced light−matter interactions. In the mid-IR, this property can be leveraged for chemical identification by increasing the sensitivity of IR spectroscopy, an effect known as surface-enhanced infrared absorption (SEIRA).[10−19]

Typically SRRs are arranged in periodic arrays, and their constituent structures have characteristic dimensions that are smaller than their plasmon resonant wavelength ($\lambda$) in free space. The plasmonic excitation and SEIRA enhancement in these arrays can be engineered by controlling the intrinsic properties of the resonator (i.e., composition, size, shape, etc.) and by controlling the inter-resonator interactions (i.e., pitch and arrangement). Strategies to enhance the intrinsic properties of the resonators include the fabrication of structures supporting Fano resonances[12] or leveraging metal−dielectric−metal architectures.[20] Strategies to increase the response of the resonators via inter-resonator interactions include the fabrication of tightly spaced structures,[21] which exploits near-field interactions to provide enhanced fields between neighboring structures, or the fabrication of arrays with spacing close to the resonators' effective plasmon resonant wavelength to enable the coherent and collective excitation of plasmonic structures.[14,22] For a given nanostructure characterized by plasmon resonant wavelength ($\lambda$) and arranged in a 2D array, four different interaction regimes are possible as a function of the pitch. (i) If $\boldsymbol{p} \gg \lambda/n_{\mathrm{eff}}$, where $n_{\mathrm{eff}}$ is the effective refractive index, the long-range inter-resonator interactions are weak and the resonators can be considered as isolated. (ii) If $\boldsymbol{p} \approx \lambda/n_{\mathrm{eff}}$, diffractive far-field interactions between the nanostructures in the array may create constructive interference, leading to collective modes characterized by sharp plasmonic resonances and typically high sensitivity.[14,22] (iii) If $\boldsymbol{p} < \lambda/n_{\mathrm{eff}}$ but with the structures still

**Received:** August 24, 2015
**Published:** December 15, 2015

  

DOI: 10.1021/acsphotonics.5b00466
*ACS Photonics* 2016, 3, 87−95

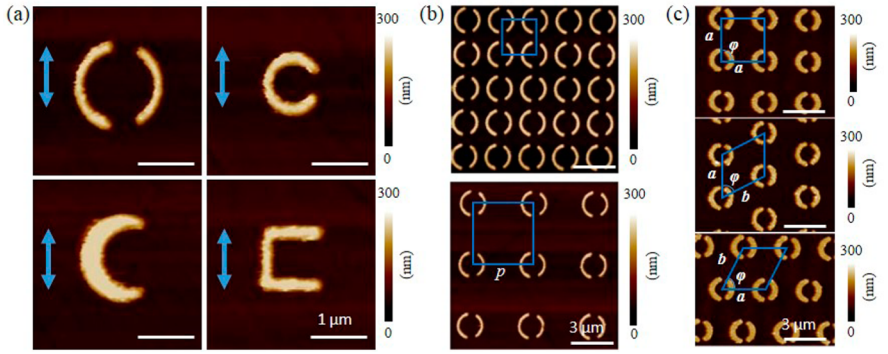


**Figure 1.** (a) AFM images for isolated ($p$ = 10 $\mu$m) plasmonic resonators of different shapes: A-SRR (top left), Cr-SRR (bottom left), C-SRR (top right), and U-SRR (bottom right). Arrows show the electric field polarization of the incident IR laser. (b) AFM images for A-SRR arrays with different pitches: 2.0 $\mu$m (top) and 3.6 $\mu$m (bottom). (c) AFM images of A-SRR arrays with different unit cell arrangements: square (top), vertically shifted centered rectangular (middle), and horizontally shifted centered rectangular (bottom). The blue shapes represent the unit cell of each array.

well separated such that the near-field interactions are negligible, the long-range inter-resonator interactions typically reduce the resonator cross-section due to destructive interference. (iv) if $\boldsymbol{p} < \lambda/(10n_{\text{eff}})$, the near-field interactions become important and can also give rise to high sensitivity.[21]

Theoretical modeling plays a primary role in the engineering of these materials because the subdiffraction confinement of plasmons, in typically closed packed arrays, challenges diffraction-limited techniques to discriminate the properties stemming from the individual resonators and from the collective response of the array. In the mid-IR the role of inter-resonator interactions has been highlighted in a few studies.[14,23,24] For example, SRR arrays with different pitches have been measured in the far field[25−27] and their response was explained by the magnetoelectric point scattering theory.[28,29] This fully analytical model accounts for the inter-resonator interactions via the electric and magnetic dipole moments, induced by light excitation.

In this regard, the extinction cross section ($\sigma_{\text{ext}}$) of isolated SRRs has been measured in the near-IR by the spatial modulation technique[27,30] or in the visible by Fourier microscopy,[31] but we are not aware of similar studies in the mid-IR. In the mid-IR, high-resolution images of the near field of plasmonic nanomaterials have been obtained by scanning scattering near-field optical microscopy (s-SNOM)[32−35] and by photothermal induced resonance (PTIR)[10,36,37] techniques. Recent reviews discussing the state of the art of these techniques can be found elsewhere.[38,39] PTIR[40−42] combines the resolution of atomic force microscopy (AFM) with the specificity of absorption spectroscopy in both the mid-IR and visible ranges.[43] PTIR has recently attracted attention because, in addition to images of the near-field, the nanoscale PTIR spectra provide a quantitative measure of the local SEIRA enhancement.[10,37] PTIR is also finding increasingly wider application in materials science[44−49] and biology.[50,51] The main goal of this paper is to exploit the PTIR method to single out and measure the SEIRA response deriving from specific plasmonic resonators in closely packed arrays and to evaluate whether their response is positively or negatively affected by the interactions with neighboring resonators.[21] Here, the near-field SEIRA hot-spot intensities are measured for SRRs of different shapes—asymmetric (A-SRR), crescent-shaped (Cr-SRR), "C"-shaped (C-SRR), and "U"-shaped (U-SRR)—that are either isolated or organized in periodic arrays with different pitches and arrangements. The results are compared with far-field ensemble measurements and with magnetoelectric point scattering calculations. The range of pitches studied in this work include the case of the isolated resonators and $\boldsymbol{p} < \lambda/n_{\text{eff}}$, approaching the limit where the near-field interactions become important but do not include the case of the coherent excitation of plasmonic arrays ($\boldsymbol{p} \approx \lambda/n_{\text{eff}}$);[14,22] see discussion. Results show that for the isolated resonators the A-SRR geometry provides the strongest SEIRA hot spots. For U-SRR arranged in square lattice arrays with different pitches, the near-field SEIRA enhancement of each resonator increases as a function of the pitch, in agreement with theoretical calculations of the resonator's extinction cross section ($\sigma_{\text{ext}}$), which also increases with the pitch. Although the inter-resonator interactions reduce the resonators' intrinsic $\sigma_{\text{ext}}$, the higher resonator density of closely packed arrays overcompensates the reduction of $\sigma_{\text{ext}}$ and provides the stronger response in the far field. In contrast, the locally measured SEIRA enhancement in A-SRR arrays is a nonmonotonic function of the pitch because of the constructive hot-spot overlap in the most closely packed array (i.e., the near-field interactions overcompensate the smaller $\sigma_{\text{ext}}$, typical of arrays with smaller pitches). Finally, by analyzing arrays composed of resonators of the same size, shape, and density but with different unit cell arrangements, the PTIR data show that the perturbation introduced by the second-order inter-resonator interactions on the near-field SEIRA enhancement is small.

## SAMPLE PREPARATION

To enable PTIR measurements, the resonators were fabricated on zinc selenide right-angle prisms by electron-beam lithography and lift-off using custom adaptors;[41] see Experimental Section for details. To discriminate the contributions to near-field SEIRA enhancement stemming from the constituent resonators (i.e., size and shape) from the ones stemming from the inter-resonator interactions (i.e., spacing and arrangement) in periodic SRR arrays, three sets of samples were fabricated (see Figure 1). The effect of the resonator shape on the near-field SEIRA enhancement was evaluated with a set of samples consisting of resonators of different shapes separated by a large pitch (10 $\mu$m) so that the inter-resonator interactions can be considered negligible. Hereafter we will refer to these samples as "isolated resonators". Because the resonant wavelengths of plasmonic structures are a function of the nanostructure size and shape, resonators with different shapes of a given characteristic size typically display different resonant wavelengths. Consequently, to compare the near-field enhancements of resonators with


DOI: 10.1021/acsphotonics.5b00466
ACS Photonics 2016, 3, 87−95

different shapes displaying resonances in approximately the same spectral region, we choose resonators of different sizes (Figure 1a). The dimensions of the resonators as measured by AFM are summarized in Table 1. The thickness of all the gold resonators

**Table 1. Characteristic Dimensions of the Isolated Resonators As Measured by AFM[a]**

| shape | characteristic dimension ($\mu$m) | resonance wavelength ($\mu$m) | Q-factor |
|---|---|---|---|
| A-SRR | 1.75 ± 0.05 | 8.85 ± 0.05 | 13.9 ± 0.5 |
| Cr-SRR | 1.65 ± 0.05 | 9.05 ± 0.05 | 5.1 ± 0.3 |
| C-SRR | 1.20 ± 0.05 | 9.00 ± 0.05 | 5.7 ± 0.3 |
| U-SRR | 1.15 ± 0.05 | 9.70 ± 0.05 | 3.6 ± 0.3 |

[a]A-SRR (outer diameter), Cr-SRR (outer diameter), C-SRR (outer diameter), and U-SRR (lateral dimension), respectively. Plasmon resonant wavelength as measured by FTIR for square arrays composed of resonators of the same size and with pitches of approximately twice the characteristic dimensions. The isolated resonators ($p$ = 10 $\mu$m) were too sparse to yield a measurable far-field FTIR spectrum for a direct comparison. The uncertainties in the resonators' dimensions represent a single standard deviation in the measurements on nominally identical resonators. The uncertainty in the plasmon resonant wavelengths and Q-factors represents a single standard deviation from Lorentzian fitting of FTIR resonance peaks.

was 180 ± 10 nm, as measured by AFM. To study the inter-resonator dipolar interactions, a second set of samples consisting of seven square arrays composed of resonators with the same sizes and shapes as the isolated resonators but with different pitches ($p$) were fabricated (28 samples total). As a representative example, Figure 1b shows the AFM images of two A-SRR arrays with $p$ = 2.0 $\mu$m and $p$ = 3.6 $\mu$m, respectively. Finally, to evaluate the effect of the higher order interactions on the SEIRA enhancement, a third set of samples consisting of A-SRR of the same size and shape as the isolated A-SRR organized in different arrangements—square (unit cell $a = b$, $\varphi = 90°$) and two centered rectangular (unit cell $a \neq b$, $\varphi \approx 53°$)—were fabricated (see Figure 1c). For these latter samples, the lattice constants were chosen to be approximately twice the size of the resonators (~3 $\mu$m), Figure 1c. In particular, the two centered rectangular arrays can be thought of as constructed from a square array by shifting every other column of the array vertically by a half unit cell or by shifting every other row of the array horizontally by a half unit cell, respectively. Because the resonators' density of square and centered rectangular lattices is the same, these arrays were used to evaluate the effect of higher order inter-resonator interactions on the near-field SEIRA enhancement, which should be a weak function of the near-neighbor configurations and resonators' shapes.

## RESULTS AND DISCUSSION

After fabrication, far-field Fourier transformed infrared (FTIR) spectra were recorded with an IR microscope, and nanoscale topography images of the bare resonators were obtained by an AFM microscope. Prior to the PTIR experiments, a 200 nm thick poly(methyl methacrylate) (PMMA) film was spin-coated on each sample. In the PTIR experiments, the samples were illuminated at 45° by total internal reflection from the prism side as shown in Figure 2a. In all PTIR measurements, the light polarization was in the sample plane along the direction (vertical) indicated by the arrows in Figure 1a. The absorption of a laser pulse by the sample induces heating, sample expansion, and mechanical excitation of the AFM cantilever in contact with

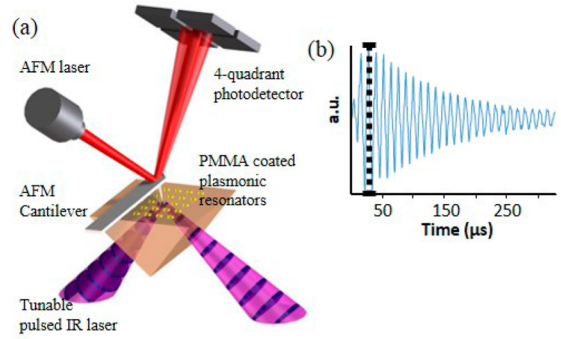


**Figure 2.** (a) Schematic of the PTIR measurement setup. (b) The PTIR signal intensity is determined by the maximum amplitude of the cantilever ring down signal (black dotted line), which is proportional to the energy absorbed by the sample.

the sample. The resulting cantilever oscillations have an amplitude that is proportional to the absorbed energy (Figure 2b) and are monitored by a four-quadrant detector. PTIR maps are obtained by illuminating the sample at a constant wavelength while scanning the AFM tip and plotting the amplitude of the tip deflection as a function of the tip location. Local infrared spectra were obtained by positioning the AFM tip in a desired location and by plotting the maximum amplitude of the tip deflection as a function of the excitation wavelength.

Figure 3a–h show pairs of topography and PTIR maps for the isolated resonators obtained illuminating the sample at 1142 $cm^{-1}$ (corresponding to the PMMA C–O stretching absorption). Because the PTIR signal is proportional to the absorbed energy and to the sample thermal expansion and is inversely proportional to the sample thermal conductivity,[41,42,47,52] the contribution of absorption in the resonators due to ohmic dissipation to the intensity of the PTIR images in Figure 3 is negligible.[10] Consequently, the PTIR images represent a direct image of the SEIRA enhancement in the near field displaying hot spots in regions where the SEIRA enhancement is most prominent. Such enhancement arises from the local electromagnetic field confinement that occurs near the gaps or terminations of the plasmonic structures. Figure 3i compares the PTIR spectra of PMMA obtained from the hot-spot locations with the spectrum of the PMMA film obtained ~100 $\mu$m away from the resonators (see Experimental Section for details). For the resonators' geometrical parameters used in this work, the PTIR spectra and maps show that the A-SRR structure provides the strongest SEIRA enhancement, followed by C-SRR and U-SRR structures and then by Cr-SRR, which displays the weakest hot spots. We define the SEIRA enhancement factor ($\Gamma$) at a given wavelength as the ratio of the PTIR intensity in the hot spot with respect to the PTIR intensity in the PMMA film obtained 100 $\mu$m away from the resonators. The values of $\Gamma$ obtained in the experiments are a function of the electromagnetic field confinement, which is related to the resonator's quality factor (Q-factor),[53] convoluted with the lateral resolution of the PTIR experiments (~100 nm). The range of $\Gamma$ measured in this work (from ~3 to ~11, see inset of Figure 3i) may appear much lower than record values ($10^4$–$10^5$), estimated for monolayer samples coating plasmonic antennas.[14] However, for monolayer samples, $\Gamma$ represents the average SEIRA enhancement within the volume of the monolayer in the hot-spot location (typically 1 to 10 $nm^3$). In the PTIR experiments, $\Gamma$ is an average over the whole volume probed under the tip (i.e., 1.6 × $10^6$ $nm^3$, assuming 100 nm resolution), suggesting a considerably high enhancement in


DOI: 10.1021/acsphotonics.5b00466
ACS Photonics 2016, 3, 87–95

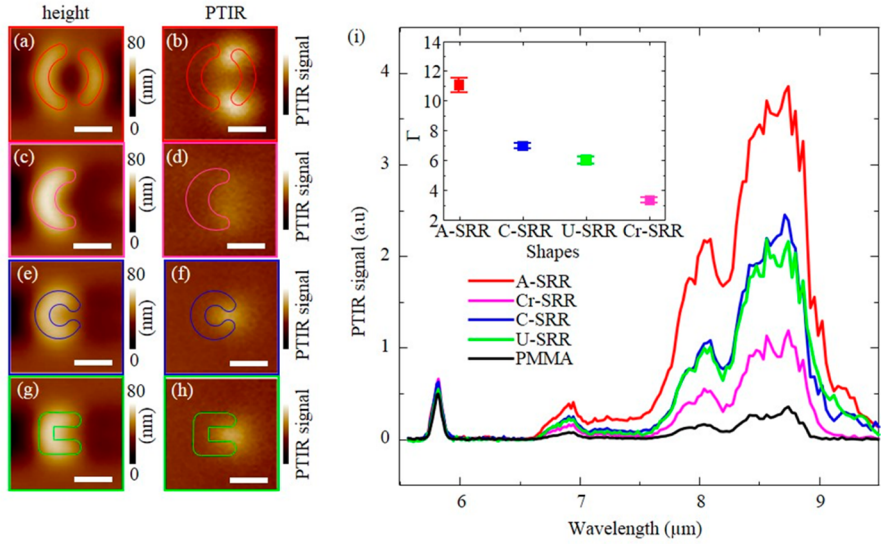


**Figure 3.** Isolated ($p$ = 10 $\mu$m) plasmonic resonators. (a–h) Pairs of simultaneously obtained AFM height (left) and PTIR (right) images for each resonator shape: A-SRR (a, b), Cr-SRR (c, d), C-SRR (e, f), and U-SRR (g, h). PTIR images were obtained by illuminating the sample at 8.75 $\mu$m (1142 cm$^{-1}$), corresponding to the C–O stretching of PMMA. The resonators' outlines were drawn based on AFM topography images obtained before coating the samples with a PMMA film. All PTIR images are displayed with a common intensity scale, and all scale bars are 1 $\mu$m. (i) The PTIR spectra from the hot-spot locations of panels b, d, f, and h are compared with the spectrum of the PMMA film obtained away from the resonators (black). The inset displays the enhancement factors ($\Gamma$) for the near-field hot spots at 8.75 $\mu$m (1142 cm$^{-1}$). The uncertainty in enhancement factor represents a single standard deviation in the measurement of the PTIR spectral intensity ratio with respect to the PMMA reference.

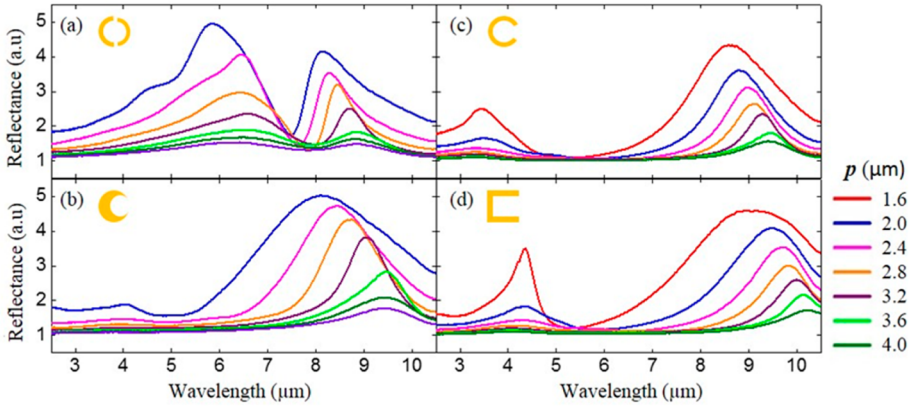


**Figure 4.** FTIR spectra of A-SRR (a), Cr-SRR (b), C-SRR (c), and U-SRR square arrays with different pitches ($p$).

proximity of the plasmonic resonator surface. The $Q$-factors of the resonators were evaluated from the far-field reflection spectra (see Table 1). According to the spectra, the A-SRR geometry displays the highest $Q$-factor (13.9 ± 0.5) followed by C-SRR, Cr-SRR, and U-SRR in decreasing order. The large $Q$-factor of the A-SRR geometry stems from the characteristic Fano resonance,[12] which provides a better confinement of the SEIRA hotspots in the near field. Because the lateral resolution of our experiments enables resolving two hot spots for A-SRR and Cr-SRR but only one for C-SRR and U-SRR, despite the larger $Q$-factor of Cr-SRR, the tighter near-field confinement in U-SRR provides a stronger local enhancement in the PTIR measurements.

For each resonator shape, the far-field reflection spectra of the uncoated arrays are displayed in Figure 4 as a function of $\boldsymbol{p}$. The plasmon resonant peaks shift to longer wavelengths (red-shift) as the inter-resonator spacing increases for all sets of samples. In the simple dipole model,[26,27] as $\boldsymbol{p}$ is increased, the electric and magnetic dipole–dipole interactions between neighboring resonators induce a red-shift or blue-shift in the plasmonic resonance, respectively.[26] Consequently, for resonators studied here, the electric dipole–dipole interactions are dominant. Additionally, a broadening of the plasmonic peak is observed for decreasing $\boldsymbol{p}$ starting from $\boldsymbol{p} \approx 3.2$ $\mu$m for all resonators' shapes, which can be explained by the super-radiant decay of the electric dipoles.[5,25,26] Those results are consistent with previous transmission experiments in the visible range.[26]

To elucidate the effects of the resonator interactions in the far and near field, we calculated the optical response of square U-SRR arrays of different pitches based on magnetoelectric point scattering theory,[28,29] which gives a full analytical model for anisotropic magnetoelectric scatterers including SRRs. In this model, SRRs are approximated by local electric and magnetic dipole moments with a dynamic polarizability in response to the incident fields. This generalized model accounts for the coupling and cross-coupling between electric and magnetic dipoles to the incident electric and magnetic fields. Commonly, dipole–quadrupole and other higher-order multipolar interactions are


DOI: 10.1021/acsphotonics.5b00466
ACS Photonics 2016, 3, 87–95

neglected in this analysis. According to this model the optical properties of a single SRR can be described by a vector whose components are the resonator's electric ($p$) and magnetic ($m$) dipole moments that are related to the incident electric ($E$) and magnetic ($H$) fields, by 6 × 6 polarizability tensor $\vec{\vec{\alpha}}$ as

$$\begin{pmatrix} p \\ m \end{pmatrix} = \vec{\vec{\alpha}} \begin{pmatrix} E \\ H \end{pmatrix} \tag{1}$$

where $\vec{\vec{\alpha}}$ should include radiation damping to satisfy the optical theorem (i.e., energy conservation).[28] The magnetoelectric point scattering theory can be extended to scatterers arranged into a two-dimensions lattice by summing all dipole−dipole interactions between SRRs in the lattice using the dyadic Green function.[29] In a periodic array, the SRR's position in the lattice is defined by the lattice vectors $R_{mn} = m\boldsymbol{a}_1 + n\boldsymbol{a}_2$ (where $m$ and $n$ are integers and $\boldsymbol{a}_{1,2}$ are the basis vectors of the array). The electric ($p_{00}$) and magnetic ($m_{00}$) dipole moments of the SRR at origin position can be expressed extending eq 1 as

$$\begin{pmatrix} p_{00} \\ m_{00} \end{pmatrix} = [\vec{\vec{\alpha}}^{-1} - \sum_{m\neq 0, n\neq 0} \vec{\vec{G}}^{0}(R_{mn}) e^{ik_{\parallel} R_{mn}}]^{-1} \begin{pmatrix} E \\ H \end{pmatrix} \tag{2}$$

where $\vec{\vec{G}}^{0}$ is the dyadic Green function and $k$ is a wave vector. For the calculations a set of parameters appropriate for our U-SRR was used: resonance wavelength of $\lambda = 10.2$ $\mu$m, volume $V = 1.35 \times 1.35 \times 0.15$ $\mu m^3$, and dimensionless polarizability coefficients ($\eta_E$, $\eta_H$, $\eta_C$) = (0.63, 0.12 0.28) as in Lunnemann et al.[29] We choose the resonance wavelength of 10.2 $\mu$m for isolated SRRs by extrapolating the resonant wavelength obtained from the far-field FTIR spectra in Figure 4d. Figure 5a shows the FTIR reflection spectra for U-SRR arrays with different pitches and the calculated $\sigma_{ext}$ per resonator (Figure 5b) obtained from the imaginary part of all 11 components of effective polarizability tensor. The extinction cross section ($\sigma_{ext}$) of isolated SRRs has been measured in the near-IR by the spatial modulation technique[27,30] or in the visible by Fourier microscopy,[31] but we are not aware of similar studies in the mid-IR. The calculated $\sigma_{ext}$ is consistent with the experimental results, which show red-shifting and narrowing of the plasmonic peak for larger $\boldsymbol{p}$. However, the maximum of the calculated $\sigma_{ext}$ increases in intensity as $\boldsymbol{p}$ increases. In contrast, the maximum of the reflection spectra decreases in intensity as the pitch increases because of the lower resonator density per unit area. After normalizing $\sigma_{ext}$ by the unit cell area of each array (Figure 5c), we obtain a good agreement with the FTIR measurements. We can summarize these results as follows: in the near field, the stronger response is obtained for isolated resonators, but in the far field the higher density of resonators in closely packed arrays overcompensates the reduction in the resonator's cross section and yields the stronger response. Using a different formalism, the reduction in the resonator cross section can be alternatively described by the destructive interference due to the excitation of resonators that are out of phase with the light scattered by neighboring resonators.[14] It is important to note that for cases where $p \approx \lambda/n_{eff}$ (not studied here) special conditions will occur as a function of the light incident angle, analyte refractive index, and wavelength, along particular in-plane directions where the resonators are all excited in phase, giving raise to larger SEIRA enhancements.[14] The collective excitation of plasmonic structure is typically characterized by very sharp plasmonic resonances that provide greater sensitivity across a narrower spectral range.[14,22] Because one of the benefits of IR spectroscopy, and the main driver of our work, is the identification of chemical composition of unknown samples, determining the particular combinations of structure, pitch, wavelength, incidence angle, and sample refractive index leading to the maximum constructive interference is not our main goal. We also note that the FTIR setup used here that illuminates the sample with a wide range of incident angles simultaneously (see Experimental Section) and the nature of the samples (continuous PMMA films), which display rapid variation of the refractive index as a function of wavelength[54] (in correspondence with absorption peaks), are not ideal for that purpose.

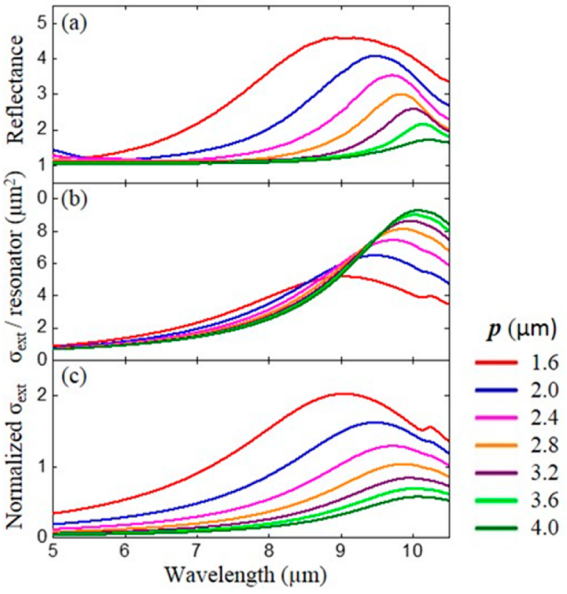


**Figure 5.** (a) FTIR spectra in U-SRR arrays (the same data in Figure 4d with different scale). (b) Theoretical calculation of the extinction cross section per resonator. (c) Theoretical calculation of the extinction cross section normalized by unit cell area of the U-SRR array.

After coating these U-SRR samples with PMMA, the PTIR images and spectra clearly show that the hot-spot intensity becomes stronger as the pitch is increased and saturates at the value for the isolated resonator (Figure 6). We define the local SEIRA enhancement factor ($\Gamma$) as the ratio of the PTIR signal intensity in the hot spot with respect to the PTIR signal intensity in the PMMA film away from the resonators. Figure 6h compares the experimentally determined values of $\Gamma$ at 8.75 $\mu$m (corresponding to PMMA vibrational absorption) with the calculated maximum value for $\sigma_{ext}$ as a function of $\boldsymbol{p}$. The good agreement between the two quantities suggests that the near-field response is directly proportional to $\sigma_{ext}$. In contrast, the near-field SEIRA enhancement in A-SRR arrays was found to be a nonmonotonic function of $\boldsymbol{p}$ (Figure 7) because for the most closely packed array (Figure 7a,b) the hot-spot intensity of neighboring resonators overlaps. The increased PTIR signal in closely packed array is also clearly observed in PTIR spectra (Figure 7e). Because the dimensionless polarizability coefficients required by the magnetoelectric point scattering theory for resonators of arbitrary shape are not available in the literature, these results highlight the utility of the PTIR analysis for characterizing the near-field response of plasmonic resonators.

PTIR data obtained on plasmonic arrays composed of resonators of the same size, shape, and density but with different arrangements are compared in Figure S1−Sn of the Supporting Information. The PTIR spectra recorded in correspondence with


DOI: 10.1021/acsphotonics.5b00466
ACS Photonics 2016, 3, 87−95

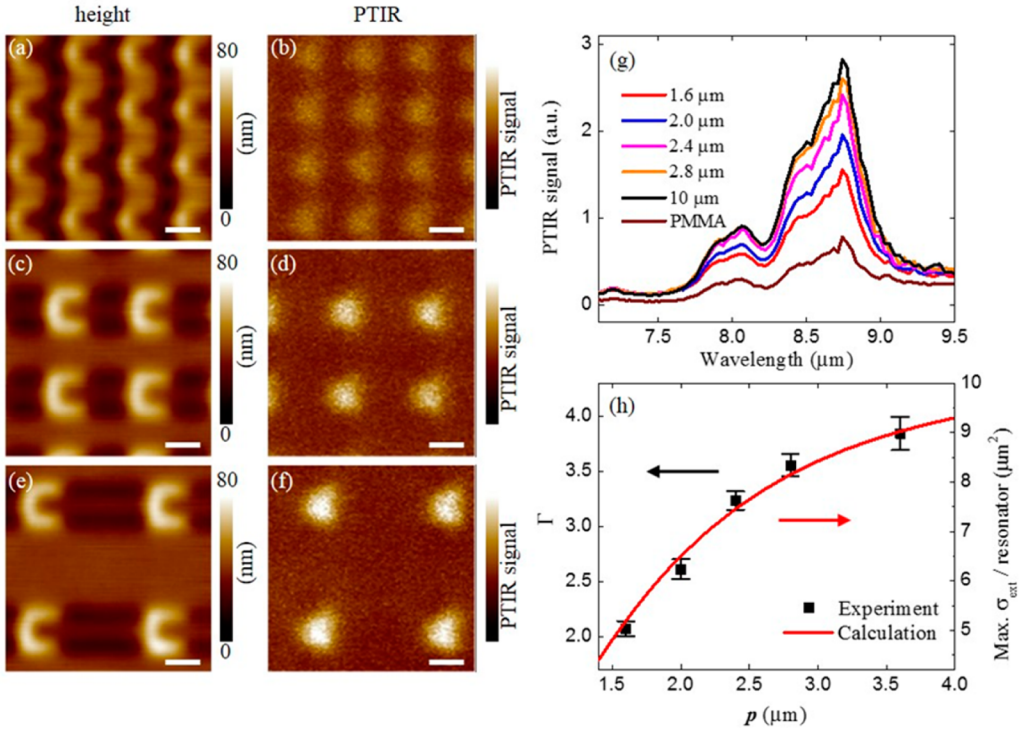


**Figure 6.** (a–f) Height (left column) and PTIR (right column) images in U-SRR arrays with pitches of 1.6 $\mu$m (a, b), 2.4 $\mu$m (c, d), and 3.6 $\mu$m (e, f). PTIR images were obtained at 8.75 $\mu$m (1142 cm$^{-1}$). PTIR images are displayed with the same intensity scale, and all scale bars are 1 $\mu$m. (g) PTIR spectra in U-SRR arrays with different pitches measured at a hot-spot location and in the bare PMMA film away from the resonators. (h) Comparison between PTIR enhancement factors ($\Gamma$) for the near-field hot spots at 8.75 $\mu$m and theoretical calculation of extinction cross section per resonator from Figure 5b. The uncertainty in enhancement factor represents a single standard deviation in the measurement of the PTIR spectral intensity ratio with respect to the PMMA reference.

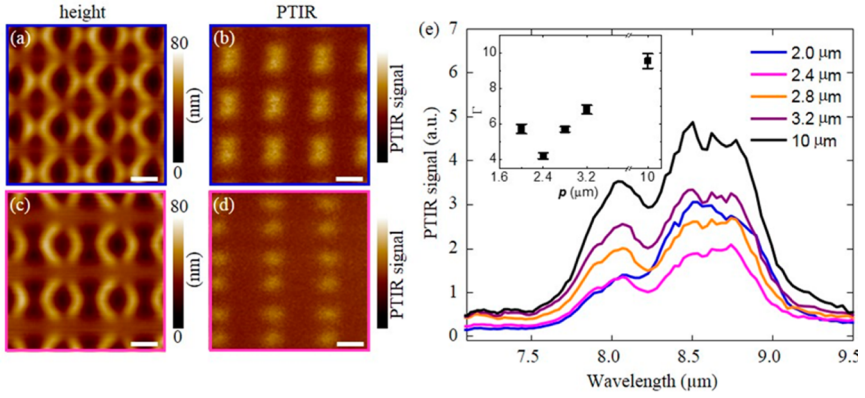


**Figure 7.** (a) Height (left column) and PTIR (right column) images in A-SRR arrays with pitches of 2.0 $\mu$m (a, b) and 2.4 $\mu$m (c, d). PTIR images are obtained at 8.75 $\mu$m (1142 cm$^{-1}$). The PTIR images are displayed with the same intensity scale, and all scale bars are 1 $\mu$m. (e) PTIR spectra in A-SRR arrays with different pitches measured at the hot-spot locations. The inset displays the enhancement factors ($\Gamma$) for the near-field hot spots at 8.75 $\mu$m. The uncertainty in enhancement factor represents a single standard deviation in the measurement of the PTIR spectral intensity ratio with respect to the PMMA reference.

the SEIRA hot-spot locations show a weak influence of the resonator arrangement on the near-field SEIRA enhancement, suggesting that the effect of the higher-order interactions between the resonators should be small and that the magnetic scattering theory provides a good approximation to describe the optical response of these resonators.

## CONCLUSION

SRR arrays with different shapes, pitches, and arrangements displaying plasmonic resonances in the mid-IR were fabricated and measured in the near and far field. The PTIR technique was used to measure SEIRA enhancement maps and spectra in the near field. Results for isolated resonators show that that the near-field enhancement is strongly dependent on the shape of the SRR. In the conditions of the PTIR experiments (45° incident light from the dielectric side) A-SRRs show the strongest near-field SEIRA enhancement. Calculations for U-shaped resonators arranged in a square lattice show that the inter-resonator dipole–dipole interactions in close-packed arrays reduce the extinction cross section per resonator. Consistently, PTIR spectra and maps show that the near-field SEIRA enhancement increases as a


DOI: 10.1021/acsphotonics.5b00466
ACS Photonics 2016, 3, 87–95

function of the pitch saturating to the case of the isolated resonator. Far-field FTIR ensemble spectra show that the higher density of resonators in arrays with a smaller pitch over-compensates the reduction in the resonator cross section and provides the strongest response. For A-SRR square arrays, the near-field SEIRA enhancement is a nonmonotonic function of the pitch thanks to the overlap of hot spots belonging to neighboring resonators for arrays with a small pitch. These results highlight the merits of the PTIR measurements for evaluating the contributions of individual resonators and inter-resonator interactions to the SEIRA enhancement in the near field.

## EXPERIMENTAL SECTION

**Nanostructure Fabrication.** All chemicals were used as received without further purification. Resonator arrays were fabricated directly on ZnSe right-angle prisms, which were cleaned in an ultrasonic bath with acetone (1 min) and isopropyl alcohol (1 min) followed by oxygen plasma cleaning (15 min). A PMMA bilayer (250 and 300 nm) positive electron beam resist was spun (25 Hz) using a custom adaptor[41] and cured (140 °C for 15 and 30 min, respectively) before depositing an aluminum charge dissipation layer (30 ± 5 nm) with an electron-beam evaporator. The resonator arrays were written with electron beam lithography (100 kV accelerating voltage, 1000 $\mu C/cm^2$ electron beam dose) using another custom adaptor.[41] The aluminum layer was then removed using an aqueous tetramethylammonium hydroxide (2.4% volume fraction) solution, and the pattern was developed in a mixture of methyl isobutyl ketone and isopropyl alcohol. A thin chromium adhesion layer (~5 nm) and a gold layer (180 ± 10 nm) were deposited by electron-beam deposition. Finally, the ASRR arrays were obtained after lift-off of inin *N*-methyl-2-pyrrolidone PMMA remover. All arrays have dimensions of 300 $\mu$m by 300 $\mu$m. After preliminary characterization, a 200 nm PMMA film was spin coated on the resonator arrays.

**FTIR Characterization.** Far-field Fourier transform infrared reflectance spectra were recorded with an IR microscope equipped with a 36× reverse Cassegrain objective (NA = 0.52), which illuminates the sample from all directions at angles between 15° and 30° from the sample normal. Light polarization was controlled with a wire grid polarizer to have the electric field linearly polarized in the direction (vertical) indicated by the arrows in Figure 1a for all samples. The spectra were collected through a fixed aperture of 200 $\mu$m × 200 $\mu$m. Consequently the number of resonators sampled depends on the density of the resonators in the array. A total of 128 spectra (4 $cm^{-1}$ resolution) were acquired and averaged for each sample.

**PTIR Characterization.** PTIR experiments were carried out using a commercial PTIR setup that consists of an AFM microscope operating in contact mode and a wavelength-tunable (from 2.5 to 9.76 $\mu$m) pulsed laser source (maximum energy per pulse used was 0.4 $\mu$J) The laser consists of an optical parametric oscillator based on a noncritically phase-matched $ZnGeP_2$ crystal. A set of three motorized mirrors was used to control the light polarization at the sample. Although the laser spot size at the sample is large (~30 $\mu$m), the AFM cantilever provides nanoscale spatial resolution by transducing locally the small sample expansion in large cantilever oscillations. The low repetition rate of the laser (1 kHz) assures that a new pulse excites the sample and cantilever after they have returned to equilibrium. The acquisition of the sample topography and PTIR maps was synchronized so that each AFM pixel corresponds to a PTIR pixel obtained by averaging 32 consecutive laser pulses. The pixel size was 50 nm × 50 nm in all PTIR images. PTIR spectra were obtained by averaging the cantilever deflection amplitude of 256 individual laser pulses at each wavelength to increase the signal-to-noise ratio. The spectra were obtained by tuning the laser at intervals of 4 $cm^{-1}$. PTIR spectra of 4 to 8 individual hot spots were measured and averaged to compare the near-field SEIRA enhancements of different SRR arrays. Because the two A-SRR centered rectangular arrays were fabricated separately on different substrates, as opposed to the other sample groups, which were obtained together in one fabrication process, a normalization procedure of the hot-spot intensity was necessary to account for sample-to-sample thickness variation. First, to account for sample-to-sample PMMA thickness variations, the PMMA spectrum obtained 100 $\mu$m away from the resonators from one sample was used as a reference and the equivalent PMMA spectrum from the other sample was normalized in its respect to yield a spectral scaling factor. To compensate the sample to sample variations for the gold thickness and shape, the spectra were further normalized with respect to the hot-spot intensity of nominally identical square arrays on each sample. Commercially available 450 $\mu$m long silicon contact-mode AFM probes with a nominal spring constant between 0.07 and 0.4 N/m were used for this study.

## ASSOCIATED CONTENT

### Supporting Information

The Supporting Information is available free of charge on the ACS Publications website at DOI: 10.1021/acsphotonics.5b00466.

Additional PTIR images and spectra (PDF)

## AUTHOR INFORMATION

### Corresponding Author

*E-mail: andrea.centrone@nist.gov.

### Notes

The authors declare no competing financial interest.

## REFERENCES

(1) Veselago, V. G. The electrodynamics of substances with simultaneously negative values of $\varepsilon$ and $\mu$. *Sov. Phys.* **1968**, *10*, 509−514.
(2) Pendry, J. B.; Holden, A. J.; Robbins, D. J.; Stewart, W. J. Magnetism from conductors and enhanced nonlinear phenomena. *IEEE Trans. Microwave Theory Tech.* **1999**, *47*, 2075−2084.
(3) Pendry, J. B. Negative refraction makes a perfect lens. *Phys. Rev. Lett.* **2000**, *85*, 3966−3969.
(4) Schurig, D.; Mock, J. J.; Justice, B. J.; Cummer, S. A.; Pendry, J. B.; Starr, A. F.; Smith, D. R. Metamaterial electromagnetic cloak at microwave frequencies. *Science* **2006**, *314*, 977−980.
(5) Linden, S.; Enkrich, C.; Wegener, M.; Zhou, J. F.; Koschny, T.; Soukoulis, C. M. Magnetic response of metamaterials at 100 terahertz. *Science* **2004**, *306*, 1351−1353.
(6) Shalaev, V. M. Optical negative-index metamaterials. *Nat. Photonics* **2007**, *1*, 41−48.
(7) Lahiri, B.; McMeekin, S. G.; Khokhar, A. Z.; De la Rue, R. M.; Johnson, N. P. Magnetic response of split ring resonators (SRRs) at visible frequencies. *Opt. Express* **2010**, *18*, 3210−3218.
(8) Enkrich, C.; Wegener, M.; Linden, S.; Burger, S.; Zschiedrich, L.; Schmidt, F.; Zhou, J. F.; Koschny, T.; Soukoulis, C. M., Magnetic metamaterials at telecommunication and visible frequencies. *Phys. Rev. Lett.* **2005**, *95*.10.1103/PhysRevLett.95.203901
(9) Lahiri, B.; Khokhar, A. Z.; De La Rue, R. M.; McMeekin, S. G.; Johnson, N. P. Asymmetric split ring resonators for optical sensing of organic materials. *Opt. Express* **2009**, *17*, 1107−1115.



DOI: 10.1021/acsphotonics.5b00466
*ACS Photonics* 2016, 3, 87−95

(10) Lahiri, B.; Holland, G.; Aksyuk, V.; Centrone, A. Nanoscale imaging of plasmonic hot spots and dark modes with the photothermal-induced resonance technique. *Nano Lett.* **2013**, *13*, 3218−3224.
(11) Cubukcu, E.; Zhang, S.; Park, Y. S.; Bartal, G.; Zhang, X. Split ring resonator sensors for infrared detection of single molecular monolayers. *Appl. Phys. Lett.* **2009**, *95*.04311310.1063/1.3194154
(12) Wu, C. H.; Khanikaev, A. B.; Adato, R.; Arju, N.; Yanik, A. A.; Altug, H.; Shvets, G. Fano-resonant asymmetric metamaterials for ultrasensitive spectroscopy and identification of molecular monolayers. *Nat. Mater.* **2012**, *11*, 69−75.
(13) Bukasov, R.; Shumaker-Parry, J. S. Silver Nanocrescents with Infrared Plasmonic Properties As Tunable Substrates for Surface Enhanced Infrared Absorption Spectroscopy. *Anal. Chem.* **2009**, *81*, 4531−4535.
(14) Adato, R.; Yanik, A. A.; Amsden, J. J.; Kaplan, D. L.; Omenetto, F. G.; Hong, M. K.; Erramilli, S.; Altug, H. Ultra-sensitive vibrational spectroscopy of protein monolayers with plasmonic nanoantenna arrays. *Proc. Natl. Acad. Sci. U. S. A.* **2009**, *106*, 19227−32.
(15) Le, F.; Brandl, D. W.; Urzhumov, Y. A.; Wang, H.; Kundu, J.; Halas, N. J.; Aizpurua, J.; Nordlander, P. Metallic nanoparticle arrays: a common substrate for both surface-enhanced Raman scattering and surface-enhanced infrared absorption. *ACS Nano* **2008**, *2*, 707−718.
(16) Pucci, A.; Neubrech, F.; Weber, D.; Hong, S.; Toury, T.; de la Chapelle, M. L. Surface enhanced infrared spectroscopy using gold nanoantennas. *Phys. Status Solidi B* **2010**, *247*, 2071−2074.
(17) Chen, K.; Adato, R.; Altug, H. Dual-band perfect absorber for multispectral plasmon-enhanced infrared spectroscopy. *ACS Nano* **2012**, *6*, 7998−8006.
(18) Huck, C.; Neubrech, F.; Vogt, J.; Toma, A.; Gerbert, D.; Katzmann, J.; Hartling, T.; Pucci, A. Surface-Enhanced Infrared Spectroscopy Using Nanometer-Sized Gaps. *ACS Nano* **2014**, *8*, 4908−4914.
(19) Abb, M.; Wang, Y. D.; Papasimakis, N.; de Groot, C. H.; Muskens, O. L. Surface-Enhanced Infrared Spectroscopy Using Metal Oxide Plasmonic Antenna Arrays. *Nano Lett.* **2014**, *14*, 346−352.
(20) Chae, J.; Lahiri, B.; Kohoutek, J.; Holland, G.; Lezec, H.; Centrone, A. Metal-dielectric-metal resonators with deep subwavelength dielectric layers increase the near-field SEIRA enhancement. *Opt. Express* **2015**, *23*, 25912−25922.
(21) Chirumamilla, M.; Toma, A.; Gopalakrishnan, A.; Das, G.; Zaccaria, R. P.; Krahne, R.; Rondanina, E.; Leoncini, M.; Liberale, C.; De Angelis, F.; Di Fabrizio, E. 3D Nanostar Dimers with a Sub-10-nm Gap for Single-/Few-Molecule Surface-Enhanced Raman Scattering. *Adv. Mater.* **2014**, *26*, 2353−2358.
(22) Zou, S.; Janel, N.; Schatz, G. C. Silver nanoparticle array structures that produce remarkably narrow plasmon lineshapes. *J. Chem. Phys.* **2004**, *120*, 10871−10875.
(23) Liu, N.; Guo, H. C.; Fu, L. W.; Kaiser, S.; Schweizer, H.; Giessen, H. Three-dimensional photonic metamaterials at optical frequencies. *Nat. Mater.* **2008**, *7*, 31−37.
(24) Liu, N.; Kaiser, S.; Giessen, H. Magnetoinductive and Electroinductive Coupling in Plasmonic Metamaterial Molecules. *Adv. Mater.* **2008**, *20*, 4521−4525.
(25) Rockstuhl, C.; Zentgraf, T.; Guo, H.; Liu, N.; Etrich, C.; Loa, I.; Syassen, K.; Kuhl, J.; Lederer, F.; Giessen, H. Resonances of split-ring resonator metamaterials in the near infrared. *Appl. Phys. B: Lasers Opt.* **2006**, *84*, 219−227.
(26) Sersic, I.; Frimmer, M.; Verhagen, E.; Koenderink, A. F. Electric and Magnetic Dipole Coupling in Near-Infrared Split-Ring Metamaterial Arrays. *Phys. Rev. Lett.* **2009**, *103*.10.1103/PhysRevLett.103.213902
(27) Feth, N.; Konig, M.; Husnik, M.; Stannigel, K.; Niegemann, J.; Busch, K.; Wegener, M.; Linden, S. Electromagnetic interaction of split-ring resonators: The role of separation and relative orientation. *Opt. Express* **2010**, *18*, 6545−6554.
(28) Sersic, I.; Tuambilangana, C.; Kampfrath, T.; Koenderink, A. F. Magnetoelectric point scattering theory for metamaterial scatterers. *Phys. Rev. B: Condens. Matter Mater. Phys.* **2011**, *83*.10.1103/PhysRevB.83.245102
(29) Lunnemann, P.; Sersic, I.; Koenderink, A. F. Optical properties of two-dimensional magnetoelectric point scattering lattices. *Phys. Rev. B: Condens. Matter Mater. Phys.* **2013**, *88*.10.1103/PhysRevB.88.245109
(30) Husnik, M.; Klein, M. W.; Feth, N.; König, M.; Niegemann, J.; Busch, K.; Linden, S.; Wegener, M. Absolute extinction cross-section of individual magnetic split-ring resonators. *Nat. Photonics* **2008**, *2*, 614−617.
(31) Sersic, I.; Tuambilangana, C.; Koenderink, A. F. Fourier microscopy of single plasmonic scatterers. *New J. Phys.* **2011**, *13*.08301910.1088/1367-2630/13/8/083019
(32) Alonso-Gonzalez, P.; Schnell, M.; Sarriugarte, P.; Sobhani, H.; Wu, C. H.; Arju, N.; Khanikaev, A.; Golmar, F.; Albella, P.; Arzubiaga, L.; Casanova, F.; Hueso, L. E.; Nordlander, P.; Shvets, G.; Hillenbrand, R. Real-Space Mapping of Fano Interference in Plasmonic Metamolecules. *Nano Lett.* **2011**, *11*, 3922−3926.
(33) Neubrech, F.; Pucci, A.; Cornelius, T. W.; Karim, S.; Garcia-Etxarri, A.; Aizpurua, J. Resonant plasmonic and vibrational coupling in a tailored nanoantenna for infrared detection. *Phys. Rev. Lett.* **2008**, *101*, 157403.
(34) Yoxall, E.; Navarro-Cia, M.; Rahmani, M.; Maier, S. A.; Phillips, C. C. Widely tuneable scattering-type scanning near-field optical microscopy using pulsed quantum cascade lasers. *Appl. Phys. Lett.* **2013**, *103*, 213110.
(35) Grefe, S. E.; Leiva, D.; Mastel, S.; Dhuey, S. D.; Cabrini, S.; Schuck, P. J.; Abate, Y. Near-field spatial mapping of strongly interacting multiple plasmonic infrared antennas. *Phys. Chem. Chem. Phys.* **2013**, *15*, 18944−18950.
(36) Katzenmeyer, A. M.; Chae, J.; Kasica, R.; Holland, G.; Lahiri, B.; Centrone, A. Nanoscale imaging and spectroscopy of plasmonic modes with the PTIR technique. *Adv. Opt. Mater.* **2014**, *2*, 718−722.
(37) Aksyuk, V.; Lahiri, B.; Holland, G.; Centrone, A. Near-field asymmetries in plasmonic resonators. *Nanoscale* **2015**, *7*, 3634−3644.
(38) Centrone, A. Infrared imaging and spectroscopy beyond the diffraction limit. *Annu. Rev. Anal. Chem.* **2015**, *8*, 101−126.
(39) Griffiths, P. R.; Miseo, E. V. Infrared Mapping below the Diffraction Limit. In *Infrared and Raman Spectroscopic Imaging*; Wiley-VCH Verlag GmbH & Co. KGaA, 2014; pp 513−540.
(40) Dazzi, A.; Prazeres, R.; Glotin, E.; Ortega, J. M. Local infrared microspectroscopy with subwavelength spatial resolution with an atomic force microscope tip used as a photothermal sensor. *Opt. Lett.* **2005**, *30*, 2388−2390.
(41) Lahiri, B.; Holland, G.; Centrone, A. Chemical imaging beyond the diffraction limit: experimental validation of the PTIR technique. *Small* **2013**, *9*, 439−445.
(42) Katzenmeyer, A. M.; Aksyuk, V.; Centrone, A. Nanoscale infrared spectroscopy: improving the spectral range of the photothermal induced resonance technique. *Anal. Chem.* **2013**, *85*, 1972−1979.
(43) Katzenmeyer, A. M.; Holland, G.; Kjoller, K.; Centrone, A. Absorption spectroscopy and imaging from the visible through mid-infrared with 20 nm resolution. *Anal. Chem.* **2015**, *87*, 3154−3159.
(44) Dong, R.; Fang, Y.; Chae, J.; Dai, J.; Xiao, Z.; Dong, Q.; Yuan, Y.; Centrone, A.; Zeng, X. C.; Huang, J. High-gain and low-driving-voltage photodetectors based on organolead triiodide perovskites. *Adv. Mater.* **2015**, *27*, 1912−1918.
(45) Yuan, Y.; Chae, J.; Shao, Y.; Wang, Q.; Xiao, Z.; Centrone, A.; Huang, J. Photovoltaic switching mechanism in lateral structure hybrid perovskite solar cells. *Adv. Energy Mater.* **2015**, *5*, 1500615.
(46) Morsch, S.; Lyon, S.; Greensmith, P.; Smith, S. D.; Gibbon, S. R. Mapping water uptake in organic coatings using AFM-IR. *Faraday Discuss.* **2015**, *180*, 527−542.
(47) Katzenmeyer, A. M.; Canivet, J.; Holland, G.; Farrusseng, D.; Centrone, A. Assessing chemical heterogeneity at the nanoscale in mixed-ligand metal-organic frameworks with the PTIR technique. *Angew. Chem., Int. Ed.* **2014**, *53*, 2852−2856.
(48) Ghosh, S.; Kouamé, N. A.; Ramos, L.; Remita, S.; Dazzi, A.; Deniset-Besseau, A.; Beaunier, P.; Goubard, F.; Aubert, P.-H.; Remita, H. Conducting polymer nanostructures for photocatalysis under visible light. *Nat. Mater.* **2015**, *14*, 505−511.


DOI: 10.1021/acsphotonics.5b00466
*ACS Photonics* 2016, 3, 87−95

(49) Chae, J.; Dong, Q.; Huang, J.; Centrone, A. Chloride Incorporation Process in CH3NH3PbI3−xClx Perovskites via Nanoscale Bandgap Maps. *Nano Lett.* **2015**, *15*, 8114−8121.
(50) Ruggeri, F. S.; Longo, G.; Faggiano, S.; Lipiec, E.; Pastore, A.; Dietler, G. Infrared nanospectroscopy characterization of oligomeric and fibrillar aggregates during amyloid formation. *Nat. Commun.* **2015**, *6*, 7831.
(51) Dazzi, A.; Prazeres, R.; Glotin, F.; Ortega, J. M.; Al-Sawaftah, M.; de Frutos, M. Chemical mapping of the distribution of viruses into infected bacteria with a photothermal method. *Ultramicroscopy* **2008**, *108*, 635−641.
(52) Dazzi, A. PhotoThermal Induced Resonance. Application to Infrared Spectromicroscopy. In *Thermal Nanosystems and Nanomaterials*; Volz, S., Ed.; Spinger: Berlin, 2009; pp 469−503.
(53) Stockman, M. I. Nanoplasmonics: The physics behind the applications. *Phys. Today* **2011**, *64*, 39−44.
(54) Graf, R. T.; Koenig, J. L.; Ishida, H. Optical-Constant Determination of Thin Polymer-Films in the Infrared. *Appl. Spectrosc.* **1985**, *39*, 405−408.



DOI: 10.1021/acsphotonics.5b00466
*ACS Photonics* 2016, 3, 87−95